Retrospective Study for Validation and Improvement of Numerical Treatment Planning of Irreversible Electroporation Ablation for Treatment of Liver Tumors

Helena Cindrič, Panchatcharam Mariappan, Lukas Beyer, Philipp Wiggermann, Michael Moche, Damijan Miklavčič, and Bor Kos

Abstract*—*Objective: **The aims of this study were to determine the electric field threshold that best fits the local response to irreversible electroporation (IRE) ablation of hepatic tumors as seen in follow-up MRI; to numerically evaluate the heat generating effect of IRE; and to demonstrate the utility of treatment planning to improve procedures in the future.** ***Methods:*** **18 cases of hepatic tumors treated with IRE ablation were numerically reconstructed and treatment outcome was computed with a numerical treatment planning framework. Simulated ablation volumes were compared to ablation volumes segmented from 6-week follow-up MRI. Two cases with a high thermal component were selected for numerical optimization.** ***Results:*** **The best fit between segmented and simulated ablation zones was obtained at 900 V/cm threshold with the average absolute error of 5.6 $\pm$ 1.5 mm. Considerable heating was observed in 7/18 cases, where $>$50% of tumor volume experienced heating likely to cause thermal damage. In the selected two cases, thermal damage was eliminated with adjustment of applied voltages.** ***Conclusion:*** **Lesions visible on MRI 6 weeks post IRE represent areas that experienced an electric field of 900 V/cm or higher. This threshold is higher than previously reported for IRE of hepatic tumors. It is likely the 6-week follow-up period was too long and the ablation zone has already shrunk considerably, resulting in overestimation of the threshold.** ***Significance*****: We developed a sophisticated method for validation of the numerical treatment planning framework. A future prospective study can be effectively designed based on the findings of this study.**

***Index Terms*—Irreversible electroporation (IRE), liver tumors, numerical modelling, treatment planning, tumor ablation.**

I. Introduction

IRREVERSIBLE electroporation (IRE) ablation is a relatively new modality for ablation of deep-seated tumors and soft tissues [1]. Short high voltage electrical pulses are delivered to the target tissue, causing a disruption in cell membrane structural integrity and increased permeability, which leads to the loss of cell homeostasis. The affected cells cannot recover from the loss of membrane functionality and eventually die in a process similar to apoptosis [2]–[4]. IRE ablation is being evaluated for ablation of various deep-seated tumors such as in liver, pancreas, prostate and kidney [5]–[8]. Unlike in conventional ablation modalities, the success of IRE ablation does not depend on the change in target tissue temperature [1], [9]. Thus it presents an alternative treatment option in cases where the use of thermal ablation modalities is contraindicated due to risk of thermal damage to sensitive nearby structures or when the presence of heat sinks reduces ablation efficacy [7], [10], [11].

A prerequisite for successful IRE ablation is complete coverage of clinical target volume with a sufficiently high electric field (threshold). Needle electrodes are used for delivery of electric pulses and the electric field distribution in tissue mostly depends on the electrode configuration and applied voltage magnitude. Currently, the estimated threshold for IRE of hepatic tumors is around 600 V/cm, however, studies report thresholds in the range of 500-700 V/cm [12]–[15]. Furthermore, the electroporation threshold depends on the number and duration of delivered pulses – with a higher number of pulses or longer pulses a lower electric field strength will suffice [16], [17].

According to the recommendations of the current manufacturer, the electrodes need to be placed around the tumor parallel to each other and on the same depth to ease the prediction of electric field distribution. This is often difficult to achieve in practice, causing uncertainties in ablation zone appearance

Manuscript received November 20, 2020; revised February 24, 2021 and April 16, 2021; accepted April 17, 2021. Date of publication April 27, 2021; date of current version November 22, 2021. This work was supported by Slovenian Research Agency (ARRS) through the Research Program – Electroporation-based Technologies and Treatments under Grant P2-0249. *(Corresponding author: Bor Kos.)*

Helena Cindrič and Damijan Miklavčič are with the Faculty of Electrical Engineering, University of Ljubljana, Slovenia.

Panchatcharam Mariappan is with the Department of Mathematics and Statistics, Indian Institute of Technology Tirupati, India.

Lukas Beyer is with the Department of Diagnostic and Interventional Radiology, Ernst von Bergmann Hospital, Germany.

Philipp Wiggermann is with the Institute of Radiology and Nuclear Medicine, Hospital Braunschweig, Germany.

Michael Moche is with the Department for Interventional Radiology, Helios Park-Klinikum Leipzig, Germany.

Bor Kos is with the Faculty of Electrical Engineering, University of Ljubljana, Ljubljana, Slovenia (e-mail: bor.kos@fe.uni-lj.si).

This article has supplementary downloadable material available at https://doi.org/10.1109/TBME.2021.3075772, provided by the authors.

Digital Object Identifier 10.1109/TBME.2021.3075772

[18], [19]. In order to avoid undertreatment of the target tissue, voltages higher than strictly required and multiple sessions with additional electrodes or electrode retractions are often used in practice to produce a larger ablation zone. There is currently no method for real-time monitoring of ablation efficacy. In some studies on IRE ablation of pancreatic cancer a 12-15 A increase in electric current of was suggested as an indicator for successful irreversible electroporation. In order to achieve this increase in electric current additional (hundreds of) pulses are applied to tissue [20], [21]. While this method may be feasible for successful ablation in the pancreas, the implementation of the specific current increase of 12-15 A might not be an appropriate endpoint for all tumor types and locations [22]. Several experimental studies have also shown that current protocols may lead to a considerable Joule heating and thermal damage in the vicinity of electrodes. This may impact treatment safety if the electrodes are positioned in the immediate vicinity or touching certain anatomical structures susceptible to thermal damage – for example in the liver thermal damage to bile ducts can result in life threatening complications [23]–[25].

A numerical treatment planning tool that predicts ablation zone *a priori* presents an option for overcoming the uncertainties in the treatment area (especially undertreatment) and avoiding potential thermal damage to nearby critical structures. Furthermore minimizing thermal damage of targeted tissue, i. e. tumor, facilitates both immune response and faster resolution of ablated tissue. A patient specific numerical model is developed from the patient's medical imaging and a treatment plan is then prepared, completed with an optimized number and positioning of the electrodes and applied voltages. Thus complete coverage of target volume with a sufficiently high electric field is ensured, avoiding undertreatment of the target area, while (thermal) damage to surrounding tissue is minimized. The clinical practicality of numerical modelling for treatment planning has already been shown [12], [15], [26], however, further validation using clinical data and a robustness analysis of developed treatment plans are needed in order to introduce numerical treatment planning into clinical routine.

In this retrospective study, 18 cases of hepatic tumors treated with IRE ablation were numerically reconstructed and treatment outcome was computed with the numerical treatment planning framework, which was developed previously [12], [27]–[29]. Simulated ablation volumes were extracted from computed 3D electric field distribution and compared to actual ablation volume determined from follow-up MRI. The main objective of our study was to determine the electric field threshold in the numerical model, which best fits the clinical response in target tissue obtained from follow-up imaging. This would allow us to determine at which electric field threshold *in silico* we expect a complete ablation *in vivo* and therefore validate the outcome prediction of the treatment planning framework for IRE ablation of hepatic tumors. Furthermore, we investigated the thermal component of IRE ablation in our dataset and demonstrated the potential of treatment planning to ensure complete coverage of target area while avoiding thermal damage, and to improve and shorten future IRE procedures.

II. Materials and Methods

A. Case Selection Eligibility Criteria

A review of patients who underwent IRE ablation of primary and secondary liver tumors at the author's institution between 2015 and 2018 was performed. Cases were selected for the numerical study based on the availability of data for numerical reconstructions – the accessibility of pre-interventional contrast-enhanced CT (CECT), complete peri-interventional CT scans with all electrode positions visible, follow-up imaging and complete reports of delivered IRE protocols (active electrode pairs, applied voltage magnitude, number and duration of applied pulses, retraction/replacement of electrodes). A total of 18 cases were eligible for reconstruction – 12 cases of primary liver cancer (HCC) and 6 cases of various liver metastases. The tumor characteristics and procedure data for all 18 cases are available in supplementary materials in Table E4. The patient data used in this retrospective study is from clinical procedures performed in the past. All the patient data used in this study was completely anonymized and IRB approval was therefore not required according to local regulations.

B. Ablation Procedure and Follow-up

Patients underwent percutaneous irreversible electroporation ablation of primary and secondary hepatic tumors. A multiphase (arterial and portal venous phase) contrast-enhanced CT (CECT) and/or multiphase MRI was acquired up to 30 days prior to the procedure. The number of needle electrodes, insertion trajectories and placement were decided by the interventional radiologist based on pre-and peri- interventional imaging.

IRE procedures were performed with the NanoKnife system (AngioDynamics, Latham, NY, USA) using 4–6 electrodes (1.2 mm diameter, 2 cm active length) per ablation. After needle insertion, a native CT scan was taken to confirm the needle placement. Pulse parameters were defined according to AngioDynamics guidelines with applied voltage ranging from 1200 to 3000 V. Generally, 100 pulses of 90 μs were delivered per electrode pair in sequences of 10 pulses, followed by delay for recharge of the pulse generator. Delivery of each single pulse was synchronized with the absolute refractory period of patients' ECG cycle using AccuSync. The delivered current and voltage were recorded automatically by the pulse generator with a specified hardware precision of 3% [30]. The successful delivery of all pulses was considered as procedure endpoint. All procedures were performed under general anesthesia with muscle relaxation.

The first follow-up imaging was performed on the first working day after intervention with an abdominal CT and contrast enhanced T1W MRI. Consequent follow-up MRI was performed at approximately 6 week post- and 3 months post-intervention.

C. Numerical Reconstruction

Patients' pre-interventional CECT and peri-interventional native CT (showing electrode positions) were used for the numerical reconstructions of IRE procedures. First, the

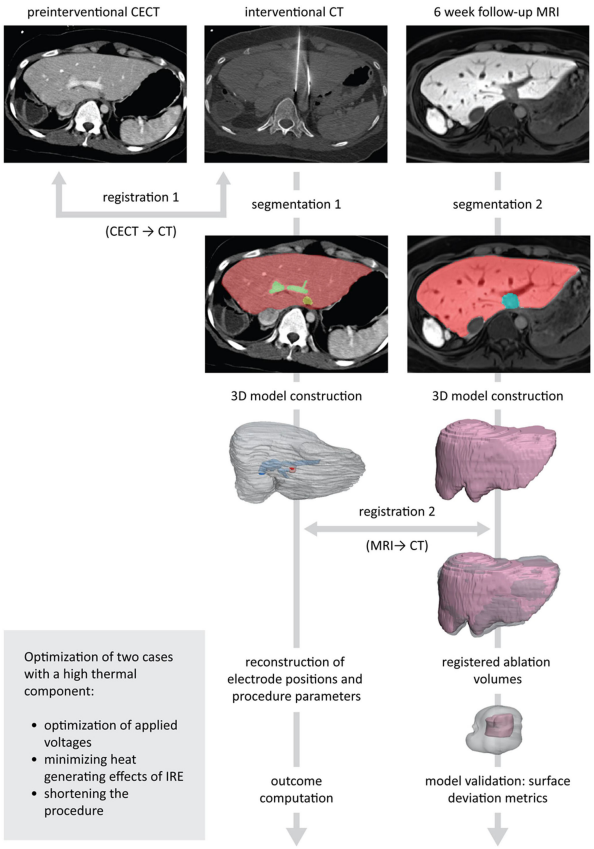

Fig. 1. Study design and steps. Three sets of patient images were used for the numerical reconstruction of each case: pre- and peri-interventional CT for the reconstruction of the IRE procedure and approximately 6 week follow-up MRI for comparison of the simulated and the actual ablation zone. All three sets had to be registered into the same imaging domain, the domain of the peri-interventional CT, which also served as the computation domain in the numerical model. Validation of the model was performed through a comparison of the simulated and the actual ablation zone segmented from follow-up MRI using surface deviation metrics.

pre-interventional CECTs were registered into the spatial domain of the peri-interventional CT, which served as the computational domain (Fig. 1). Rigid registration with mutual information criterion was selected for registration using the registration tool in ITK-SNAP software [31]. Tissues of interest – tumor volume, liver parenchyma and major blood vessels in the vicinity of the treated area (< 3 cm from tumor border) – were then manually segmented on registered CECT (Fig. 2(A)). All segmentations were performed in ITK-SNAP and were inspected and verified by an experienced radiologist.

For each patient, a 3D anatomically correct numerical model was built based on segmented tissue masks from CECT (Fig. 1). Final positions of needle electrodes were determined from peri-interventional CT (Fig. 2(B)) and introduced into the model. Treatment parameters, namely active electrode pairs, applied voltage, number and duration of delivered pulses and potential electrode re-placement or retraction (in cases where multiple sessions were required) were determined from treatment reports. Measurements of delivered currents and actual voltage of electrical pulses delivered were extracted from the NanoKnife pulse generator and used for validation of computed electric currents (Fig. 2(D)).

Treatment outcome was computed using the numerical framework for planning of electroporation based treatments [12], [27]. COMSOL Multiphysics v5.4 (Comsol Inc., Sweden) was used for numerical computations, however, the model construction and simulation set up was performed in MATLAB R2018b (MathWorks, USA) via LiveLink connector.

Electric field distribution in the target tissue is computed indirectly by solving the stationary partial differential equation for electric potential [32], [33]. The stationary model is supplemented with the modified Pennes' bioheat transfer equation solved in time domain, which includes the Joule heating term and bioheat term [34], [35]. The electrical conductivity of modelled tissues is affected by both electroporation phenomenon and heating electroporation is implemented in the model through a non-linear electric field dependent increase in tissue base electrical conductivity [36]. The thermal dependence of electrical conductivity is modelled with a constant factor of increase of 1.0%/ °C. The bioheat term of the Pennes equation represents tissue perfusion and metabolic activity, however, when electroporation occurs tissue perfusion decreases significantly due to vascular lock effect [37]. The delays after each sequence of ten pulses are an important part of the heating/cooling dynamics during IRE ablation and were therefore accounted for in our model.

The electric field distribution is calculated separately for each active electrode pair used in the procedure. The final electric field distribution *in situ* is determined by combining the maximal electric field contributions from all electrode pairs (cumulative coverage of target tissue). Thermal damage in target tissue is determined by integrating the Arrhenius kinetics equation over the treatment time period [38]. The kinetic parameters of the equation were selected to expose the most alarming thermal effects which start at temperatures above 50°C, namely, protein denaturation [39], [40]. The threshold for thermal damage was 90 % probability of cell death as determined by the integration. For each case, the results of the reconstruction consist of a final 3D electric field distribution as experienced by tissue, the temporal evolution of tissue temperature and a 3D map of thermal damage probability.

A more detailed description of the model and equations used in the computation is available in supplementary materials. All selected tissue properties and model parameters are available in supplementary materials in Tables E1 and E2. All segmented tissue masks (interventional CECT and follow-up MRI), 3D surface models of liver, tumors and segmented ablation zones, and 3D electric field distributions are available for download in the associated data repository.[1]

D. Model Validation

For each case, we extracted six isosurfaces from the 3D electric field distribution, which correspond to threshold values of 400-900 V/cm (100 V/cm steps). These simulated ablation

[1]https://doi.org/10.6084/m9.figshare.12961646.v1

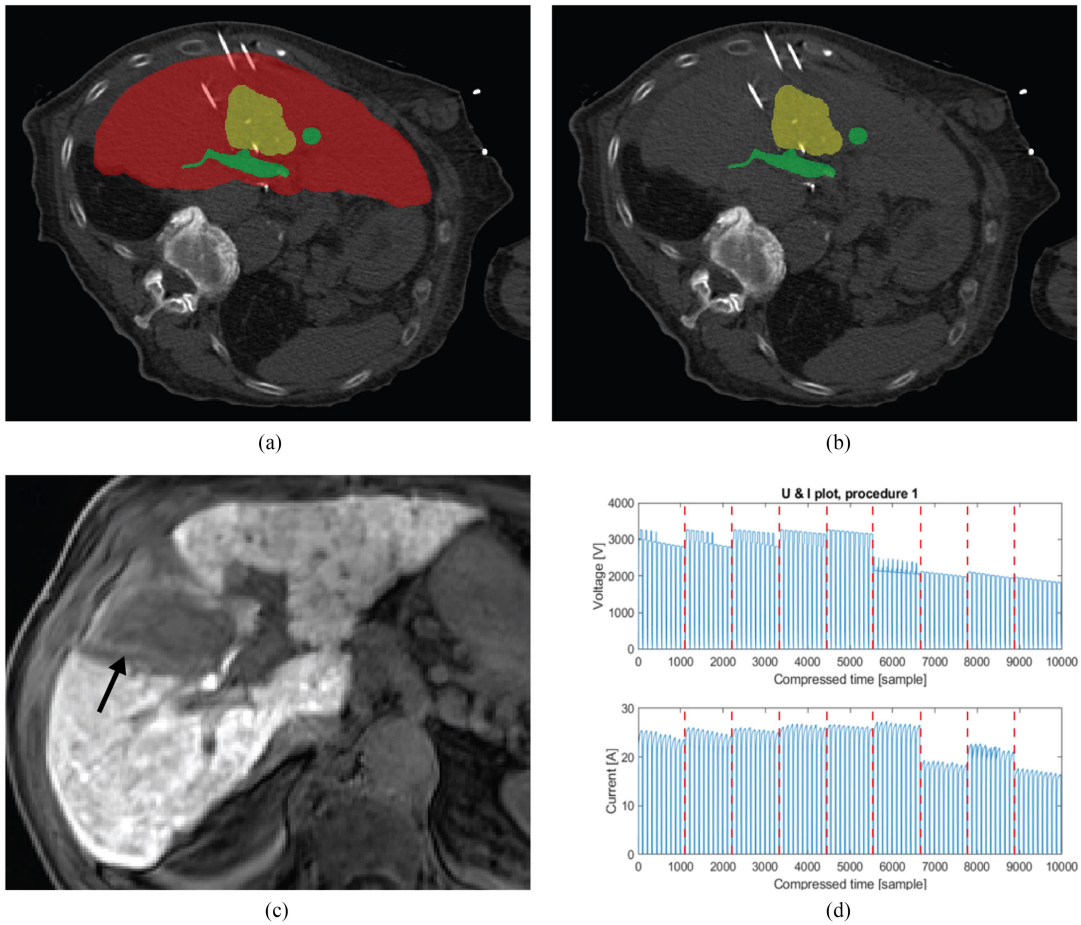

Fig. 2. An example of tissue segmentation, electrode placement and follow-up imaging for one of the reconstructed cases (case P14 in Table E4 in supplementary materials). In this particular case, the tumor was very large, therefore two consecutive sessions were performed with 2 cm electrode retraction in between sessions. A) Tissue segmentation overlay on pre-interventional CECT (yellow – tumor, green – vessels, red – liver parenchyma). B) Native interventional CT with visible needle electrode positions. C) Seven week follow-up late phase T1W MRI. Ablation zone is visible as hypo-enhanced region with a hyper-intense rim (arrow). D) An example of voltage and electric current measurements recovered from NanoKnife device. Nine electrode pairs were used in this case with 100 pulses delivered to each pair in each session. Only the first 10 pulses of each pair are shown to highlight the difference in voltage magnitude applied to different pairs – there was no voltage decrease visible in the subsequent 90 pulses. Electrode pairs are separated with dashed lines.

volumes were then compared with ablation volumes segmented from follow-up MRI. Six week follow-up T1W MRI (median 5.5 weeks, range 4–12 weeks) was chosen for model validation, since 1-day follow-up was not suitable for segmentation due to edema and poor visibility and 3-month follow-up was too long. The hepatic capsule and ablation volume (zone) were manually segmented on the MRI using ITK-SNAP software. The ablation zone is visible on the late hepatobiliary phase as a hypo-intense region with a peripheral hyper-intense rim (Fig. 2(C)).

In order to compare the segmented and simulated ablation volumes, the follow-up MRI needed to be registered into the spatial domain of peri-interventional CT (Fig. 1). Due to the multimodal nature of images, the registration was performed using hepatic capsule masks. Segmented masks from CT and MR were transformed into 3D liver models, which were then registered using Materialise 3-matic software (Materialise NV, Belgium). The registration resulted in the alignment of segmented and simulated ablation volumes to a common coordinate system on which the analysis of surface deviation between the volumes was then performed (Fig. 1). Average absolute error (AAE) was chosen as the measure of surface deviation and was calculated for each combination of segmented ablation surface and simulated ablation surface at 400-900 V/cm thresholds. AAE is a measure to find how on average two objects differ and is calculated as follows:

$$AAE = \frac{\sum_i w_i \left| d_i \right|}{\sum_i w_i} \quad . \tag{1}$$

In (1), per-face metrics are computed by trilinear interpolation from the distance level set (d) at the center of the face and weighted (w) over the area of the triangle face.

E. Statistical Analysis

The statistical analysis was performed in MATLAB using the Statistics and Machine Learning Toolbox. Difference between HCC and metastatic tumor subgroups were calculated using the

Wilcoxon rank sum test (Mann-Whitney test). Correlations between segmented ablation size and average absolute error (AAE) for both subgroups and for the whole dataset were calculated using the Spearman's rank correlation coefficient.

F. Treatment Planning/Case Optimization Example

In order to demonstrate how treatment planning could improve future IRE procedures, two cases, in which the reconstructions suggested a high percentage of thermal damage in the target tissue, were selected for optimization and development of a hypothetical treatment plan. In this study only applied voltage magnitudes were optimized.

In the first selected case, 6 electrodes were used in the original procedure, constituting 10 active electrode pairs. Retraction of the electrodes (1.5 cm) was also performed thus resulting in two successive deliveries of 100 pulses to all electrode pairs (i.e., 200 pulses delivered altogether). In the optimized plan, the original electrode placement was preserved. However, electrode retraction was omitted and longer conductive electrode tip was used instead – 3 cm as opposed to the original 2 cm tip. These additional changes were based on previous experience and were not subject to further optimization. In the second case, 6 electrodes were used in the procedure forming 10 active electrode pairs and no retraction was performed. The original electrode placement without further modifications was used in the optimized plan as well.

Optimization of applied voltage magnitudes to electrode pairs was performed in MATLAB by calculating the minimum of a nonlinear criterion function F (2). The criterion function was constructed to ensure complete IRE of clinical target volume (CTV), while minimizing IRE of the surrounding healthy tissue and preventing a large current draw. The threshold for IRE of tumor and healthy liver tissue was set to 600 V/cm according to the literature [12]–[14], [41], [42].

$$F = -1000 \cdot V_{CTV_{PP}} + 10 \cdot \frac{V_{LIVER}}{3 \cdot V_{CTV}} + \sum_{all\ pairs} f(I), \tag{2}$$

$$f(I) = 2^{I - I_{CUT}}, \tag{3}$$

In (2) $V_{CTV \cdot PP}$ stands for the fraction of CTV experiencing IRE, V_{CTV} and V_{LIVER} are the CTV and volume of healthy tissue experiencing IRE respectively, and *f(I)* is the nonlinear function representing electric current limitation (3). The contribution of *f(I)* to the criterion function F is negligible until the calculated current I exceeds the cutoff value I_{CUT} (set to 40 A in our case). If this happens, the contribution of *f(I)* rapidly increases thus eliminating the pairs that would potentially cause a high current draw. The weights in the criterion function were selected arbitrarily but with respect to individual demands for IRE.

In a single iteration of the optimization process new voltages were selected for all electrode pairs from a pool of possible values ranging from 1500 V to 3000 V (only multiples of 100 V were allowed as candidates to speed up the process). The stationary model was computed using the new voltages and the criterion function was evaluated. The process was repeated until a minimum of the criterion function was reached.

Only the computation of the stationary electric field was used in the optimization, since heating is directly dependent on delivered energy, or in other words, changing (lowering) the applied voltage will also change (lower) the delivered energy and therefore heat. The addition of heating computation in time domain would not significantly improve the accuracy of the criterion function while it would significantly increase the necessary computation resource and optimization time.

The selected voltages resulting in the function minimum were considered as the optimized treatment parameters (plan). The compete model with computation of heating in time domain was then computed to evaluate the thermal component in the optimized plan. Lastly, the percentage of volume, where the probability of thermal damage exceeded 90 %, was calculated and compared to the original results from the reconstruction.

TABLE I
COMPARISON OF MEASURED AND COMPUTED MEAN ELECTRIC CURRENTS AND ROOT MEAN SQUARED ERROR (RMSE) FOR EACH CASE

Case	Mean measured current (A)	Mean computed current (A)	RMSE (A)
P1	37.5	26.9	12.3
P2	20.9	18.7	3.8
P3	36.7	35.3	9.6
P4	30.0	29.3	9.4
P5	26.3	29.8	4.6
P6	23.3	30.6	14.0
P7	26.3	21.1	5.8
P8	27.2	29.5	5.2
P9	33.6	23.3	12.0
P10	22.8	22.1	8.8
P11	27.0	24.1	4.2
P12	26.3	28.8	3.9
P13	21.7	23.5	5.8
P14	29.0	38.2	15.0
P15	40.4	24.0	17.3
P16	28.2	23.4	5.1
P17	21.4	22.0	3.4
P18	26.8	35.3	13.3

III. RESULTS

For each reconstructed case, the computed electric current for all electrode pairs was compared to the current measurements recovered from NanoKnife pulse generator. Table I shows the mean electric current value (averaged over all active electrode pairs) and root mean squared error (RMSE) for all 18 reconstructed cases. The average relative error of the pair-to-pair comparison of measured and computed electric current is 28.9%.

Percentage of tumor volume and clinical target volume (CTV) covered with the electric field of and above a specific threshold value (400–900 V/cm) was calculated (further on referred to as

TABLE II
PERCENTAGE OF TUMOR VOLUME COVERED IN THE ELECTRIC FIELD OF (OR ABOVE) SPECIFIC THRESHOLD (400—900 V/CM) AND PERCENTAGE OF TUMOR VOLUME SUBJECTED TO THERMAL DAMAGE. MEAN, STANDARD DEVIATION, MEDIAN AND RANGE ARE CALCULATED OVER THE WHOLE DATA SET OF 18 TUMOR CASES

Coverage	Mean [%]	Standard deviation [%]	Median [%]	Range [%]
400 V/cm	97	6.2	100	76-100
500 V/cm	94	9.7	100	68-100
600 V/cm	90	13.3	98	58-100
700 V/cm	83	17.0	89	41-100
800 V/cm	75	20.0	75	32-100
900 V/cm	65	22.0	64	21-100
Thermal damage	48	32.9	37	5-100

TABLE III
PERCENTAGE OF CLINICAL TARGET VOLUME (CTV) COVERED IN THE ELECTRIC FIELD OF (OR ABOVE) SPECIFIC THRESHOLD (400—900 V/CM) AND PERCENTAGE OF CTV SUBJECTED TO THERMAL DAMAGE. MEAN, STANDARD DEVIATION, MEDIAN AND RANGE ARE CALCULATED OVER THE WHOLE DATA SET OF 18 TUMOR CASES.

Coverage	Mean [%]	Standard deviation [%]	Median [%]	Range [%]
400 V/cm	94	11.3	99	54-100
500 V/cm	90	13.6	96	47-100
600 V/cm	85	15.8	89	40-100
700 V/cm	78	17.5	78	34-100
800 V/cm	71	18.8	70	28-100
900 V/cm	64	19.6	62	22-100
Thermal damage	36	24.5	29	3-87

coverage) as well as the percentage of thermal damage. CTV is considered as tumor volume with 5 mm and 10 mm safety margin for HCC and metastases, respectively. The mean and median coverage and thermal damage were calculated (along with standard deviation and range) over all cases and are shown in Table II for tumor volume and Table III for CTV. Detailed results for each case separately are available in supplementary materials in Tables E5 and E6. According to Tables II and III the best coverage is achieved with the lowest electric field of 400 V/cm at 97% and 94% mean volume coverage for tumor and CTV respectively, followed closely by 500 V/cm threshold, where the mean volume coverage was 94 % and 90 % for tumor and CTV respectively.

At the highest studied threshold – 900 V/cm – the mean volume coverage of tumor and CTV was 65% and 64% respectively. We extracted six isosurfaces from the electric field data, which correspond to 400-900 V/cm thresholds, thus simulating different ablation volumes. We compared the simulated ablation volumes to segmented ablation volumes from 6-week follow-up MRI. Fig. 3 shows simulated ablation volumes with respect to segmented ablation volumes. Ideally, the two volumes would be the same; however, the numerically predicted size of the ablation is always larger than the ablation seen on follow-up MRI. There is only one case, where the segmented ablation was larger than the simulated ablation. For better clarity, only data for 600 V/cm and 900 V/cm electric field thresholds is shown on Fig. 3; our results indicate the best fit is achieved at 900 V/cm, however, in

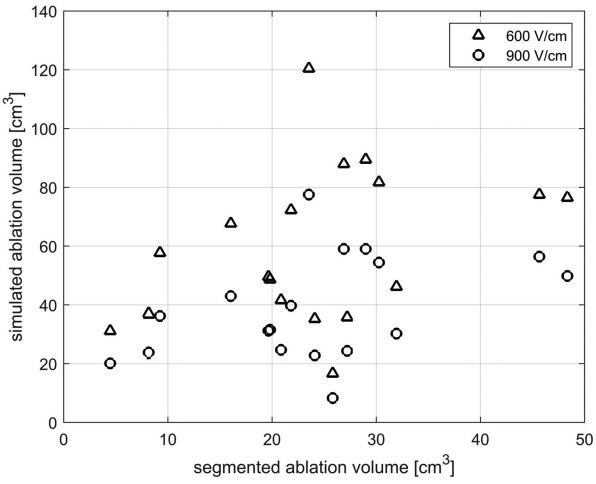

Fig. 3. Simulated ablation volume size obtained at 600 V/cm and 900 V/cm thresholds compared to the segmented ablation volume size.

TABLE IV
MEAN AND MEDIAN SURFACE DEVIATION AND RESPECTIVE DATA RANGE BETWEEN THE TWO ABLATION VOLUMES (SEGMENTED AND SIMULATED) FOR EACH OF THE SIX ELECTRIC FIELD THRESHOLDS. THE SELECTED MEASURE OF ABLATION ZONE COMPARISON IS THE AVERAGE ABSOLUTE ERROR (AAE)

Threshold	Median AAE [mm]	Standard deviation [mm]	Median AAE [mm]	Range [mm]
400 V/cm	9.4	3.4	9.8	2.6-15.6
500 V/cm	8.1	3.0	8.4	2.6-13.9
600 V/cm	7.1	2.6	7.4	3.1-12.2
700 V/cm	6.5	2.3	6.6	3.3-11.2
800 V/cm	5.9	1.8	6.0	2.8-10.6
900 V/cm	5.6	1.5	5.8	3.0-8.6

current literature lower thresholds (600-700 V/cm) for IRE of hepatic tissue are reported [12], [14], [15].

Surface deviation – average absolute error (AAE) – was calculated for each combination of segmented and simulated volumes in order to determine the best fit between the two volumes and consequently determine the *in silico* electric field value that corresponds to successful ablation of the treated tissue. AAE is lower when the segmented ablation is larger or when the electric field threshold is higher (smaller simulated ablation zone). Mean and median AAE of the overall 18 cases for each electric field threshold were calculated and are shown in Table IV along with respective standard deviations and ranges. Since the ablation zone sizes vary between the cases in our dataset, we also normalized the AAE with the diameter of the segmented ablation zone to obtain a relative value for AAE. Normalized results are presented in table E3 in Section 2 of supplementary materials. Fig. 4 shows the calculated AAE for all 18 cases with respect to segmented ablation volumes.

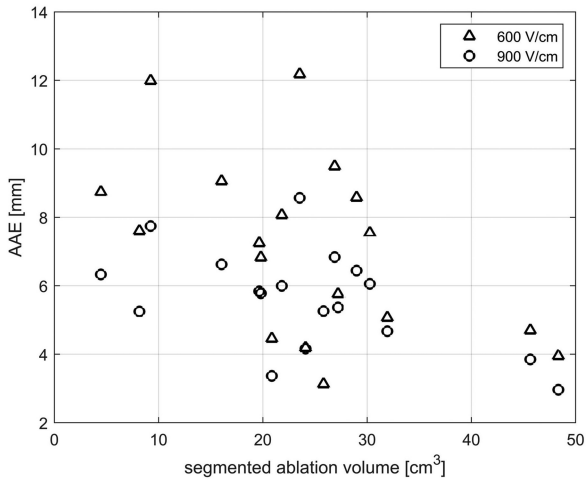

Fig. 4. Average absolute error (AAE) of surface deviation between simulated ablation volume (at 600 V/cm and 900 V/cm threshold) and ablation volume segmented from approximately 6-week follow-up MRI.

As in Fig. 3, only data for 600 V/cm and 900 V/cm electric field thresholds are shown for clarity. The results for all thresholds are provided in section 2 of the Supplementary materials.

We evaluated whether there is a statistically significant difference in AAE and electric field coverage between the metastatic and HCC tumors. The difference in calculated AAE between the two subgroups, and calculated coverage of tumor volume and CTV between the two subgroups was evaluated using the Mann-Whitney test (Wilcoxon rank sum test). No statistical difference between the two subgroups was found. Correlation between segmented ablation size and AAE for both subgroups and for the whole dataset was calculated using the Spearman's rank correlation coefficient. According to the test, there is a strong negative correlation between AAE and segmented ablation volume in the metastatic group which is statistically significant for 800 V/cm ($p = 0.033$). There is a negative correlation in the HCC group but it is not statistically significant. In the whole dataset, there is a negative correlation between AAE and segmented ablation volume, which is also statistically significant for 800 V/cm ($p = 0.047$). Correlation between segmented and simulated ablation size for both subgroups and for the whole dataset was calculated using the Spearman's rank correlation coefficient. According to the test, there is a weak positive correlation between segmented and simulated ablation size in the HCC group, but it is not statistically significant. There is no correlation in the metastatic group.

Our simulations show considerable Joule heating resulting in thermal damage of target tissue. There are 5 out of 18 cases where >50 % of CTV is thermally damaged, 7 out of 18 cases where >50 % of tumor volume is thermally damaged and 4 out of 18 cases where >90 % of tumor volume is thermally damaged (data is available in supplementary materials). The average and median volume percentage of thermal damage along with the standard deviation and data range are shown in Tables II and III for tumor volume and CTV respectively.

In our dataset, thermal damage was observed in cases that were clinically challenging and therefore more pulses were delivered to tissue – either due to electrode retraction or overall higher number of electrodes used for ablation. The numerical framework was used to design a treatment plan for two selected cases that exhibited a high thermal component with the aim of reducing thermal damage while preserving the coverage of target tissue. The threshold determined from fitting the computed results to follow-up imaging in this study was originally intended to be used in the optimization of the two selected cases as well. However, since the determined threshold is much higher than expected and reported in literature, we decided to use 600 V/cm as the threshold for IRE of tumor and healthy tissue. This value is in the middle of the range reported in literature (500-700 V/cm) and corresponds better with the clinical outcomes of our patient sample, since 14/18 cases had complete response identified 6 weeks post IRE (see Tables II and III and Tables E4-E6 in the Supplementary materials). In both cases, we were able to eliminate the thermal component completely by lowering the applied voltage magnitude. In Case 1, the voltages were lowered from the original range of 2405-3000 V to a lower range of 1700-1900 V and in Case 2 from the original span of 2310-3000 V to a lower span of 1800-2000 V. Table V shows the percentage of tumor volume and CTV experiencing thermal damage and coverage of both respective volumes with an electric field strength of 600 V/cm for both the original simulation (reconstruction) and simulation with optimized voltages. In both cases tumor coverage remained at 100%, while in Case 2 CTV coverage was 3 percentage points lower in the optimized simulation. In both cases, thermal damage of tissue was practically eliminated.

Furthermore, in Case 1, where electrode retraction was initially performed, longer electrodes were used in the simulation (3 cm instead on 2 cm) rendering retraction unnecessary and therefore potentially shortening the procedure duration. The optimization also resulted in lower electric currents in both cases. Fig. 5 shows an example of computed results for Case 2. Electric field distribution and maximum computed temperature in tissue are shown for original and optimized simulation as an overlay on the patient's peri-interventional CT images. Panels B and D show a significant reduction in tissue heating, while panels A and C show little alteration in electric field distribution and almost no change in coverage of target tissue with and electric field sufficient to cause IRE.

IV. Discussion

In this retrospective study, 18 clinical cases of IRE ablation of hepatic tumors were numerically reconstructed and treatment outcome was computed using a numerical tool for treatment planning. The aim of our study was to determine the *in silico* electric field threshold in the numerical model, that corresponds to successful ablation of target tissue *in vivo* as visible on follow-up imaging. A complete response is not necessarily considered as 100% cell death due to IRE alone. There are additional mechanisms contributing to tumor eradication, for example immune response and vascular lock, which are still being investigated [43]–[47]. Furthermore, electric field threshold should not be

TABLE V
PERCENTAGE OF TUMOR VOLUME AND CTV EXPERIENCING THERMAL DAMAGE AND COVERAGE WITH AN ELECTRIC FIELD OF 600 V/CM IN THE ORIGINAL SIMULATIONS (RECONSTRUCTIONS) AND THE OPTIMIZED SIMULATIONS

	Thermal damage				Coverage with 600 V/cm			
	Tumor volume		CTV		Tumor volume		CTV	
	original	optimized	original	optimized	original	optimized	original	optimized
Case 1	92 %	0 %	70 %	0 %	100 %	100 %	100 %	100 %
Case 2	90 %	4.6 %	63 %	2.5 %	100 %	100 %	99 %	96 %

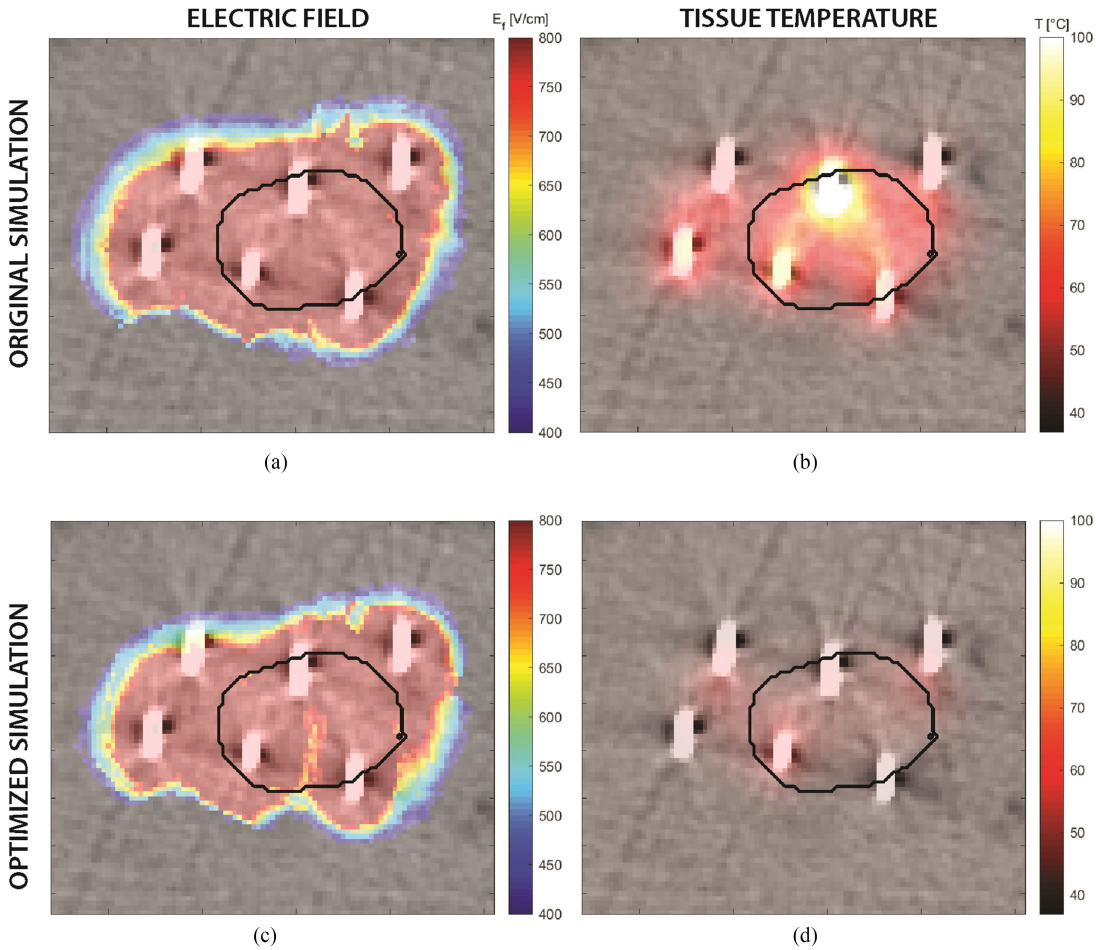

Fig. 5. Results of numerical optimization for Case 2. Computed electric field distribution and tissue temperature are represented as an overlay on patient's peri-interventional CT with six visible needle electrodes. Tumor volume is outlined in black. Panels A and B show the results of the original simulation (reconstruction). Computation indicates considerable heating, resulting in almost complete thermal ablation of tumor volume (see Table V). Temperatures around the electrodes reach up to 100 °C. Panels C and D show results after optimization of applied voltages. Tissue coverage with sufficiently high electric field remains mostly unaffected and should not negatively affect treatment success (A, C) while tissue heating is practically eliminated (B, D).

mistaken with the voltage-to-distance ratio used for calibration of delivered voltage magnitude, recommended by manufacturers of pulse generators, which has the same unit of V/cm. The electric field in our model is considered as the local electric field as experienced by cells/tissue *in situ*.

For each case, six simulated ablation volumes were extracted, corresponding to *in silico* electric field thresholds of 400–900 V/cm, and compared to ablation volumes segmented from follow-up MRI acquired approximately 6 weeks after IRE procedure. The chosen metric for ablation zone comparison was surface deviation calculated as an average absolute error (AAE). In a study by Moche *et al*. [48] a similar approach was employed to evaluate the integrability of the simulation tool for prediction of radiofrequency ablation (RFA) zones in the liver. The authors report a mean AAE of 3.4 mm $\pm$ 1.7 mm that was considered accurate enough for clinical demands. In our study, the lowest mean AAE was 5.6 mm $\pm$ 1.5 mm (standard deviation) for simulated ablation volume at 900 V/cm. It is important to note that [48] was a prospective study accounting also for the computational

demands, therefore a better correlation between computed and segmented volumes is expected than in a retrospective study.

Based on existing literature we know that a 900 V/cm threshold is higher than what is required for complete ablation of hepatic tissue with irreversible electroporation. The threshold for IRE of hepatic tumors is estimated to be somewhere between 500–700 V/cm [12]–[14], [41], [42]. With longer pulses or higher number of pulses, lower amplitudes are needed for the same fraction of electroporated cells [16], [17]. An increase in tissue temperature, which is the result of Joule heating during IRE, presumably also decreases the threshold for electroporation [35]. However, if we observe our data at lower thresholds, there is an even larger deviation between segmented and simulated ablation volumes, with simulated volumes being larger than segmented volumes. There are several possible reasons for this discrepancy. As opposed to RFA where the necrotic tissue is easily demarcated from viable tissue and its appearance on follow-up imaging does not change within the studied time frame, the healing dynamics (and consequential shrinkage) of electroporated tissue make the determination of actual ablation zone size on follow-up imaging difficult. It is therefore difficult to determine with certainty the region where apoptotic and necrotic cell death due to irreversible electroporation occur, which presumably contributes to a higher error in surface deviation when compared to the study on RFA. Furthermore, it is most likely that the 6-week follow-up period was too long and the ablation zone has already shrunk considerably. It is possible that a part of the lesion visible on 6-week follow-up represents thermal damage; however, it is practically impossible to distinguish between thermal necrosis and IRE apoptosis/necrosis on the MRI.

Recent studies on MRI findings after IRE ablation of liver metastases [49] and HCC [50] have shown that the ablation zone shrinks rapidly in size in the first 2–4 weeks after the procedure. Barabasch *et al*. [49] report an increase in ablation size in the first 24h after IRE with the mean ablation size being 836% of target lesion size one day after IRE. In the two weeks after the IRE procedure, a rapid decrease in ablation size was observed and a moderate decrease was observed afterwards. Furthermore, the rim enhancement visible on T1w and T2w MRI disappeared within 6 weeks in 21 out of 37 patients in the study. Padia *et al*. [50] also report a marked decrease of ablation zone size especially in the first 4 weeks after IRE procedure. The authors point out that early MRI (1 day post-IRE) may overestimate the appearance of the ablation zone, since both reversibly and irreversibly electroporated tissue may accumulate the gadolinium contrast agent, if the latter is present before the delivery of pulses [51].

One of the main advantages of irreversible electroporation is the preservation of the extracellular matrix and connective tissue. This quality promotes the use of electroporation in the vicinity of sensitive anatomical structures and also enables healing of treated tissue. The healing dynamics, however, are patient specific and are closely connected to the health of the liver organ and presumably also depend on patients' age and overall health status. The healing ability of cirrhotic liver is distinctively decreased which suggests the shrinking of the ablation zone might be slower in cases with cirrhotic liver (common in HCC cases) than in cases where the liver organ tissue is healthy (common in metastatic disease). Our results, however, did not show a statistically significant difference between the healthy (metastases) and cirrhotic (HCC) liver group. Although this may also be due to small sample size – 6 cases of metastases versus 12 cases of HCC. Animal experiments show fast resolution of IRE tissue within two weeks from procedure. However, two electrodes and a variety of pulse protocols were used in the experiments, resulting in a less pronounced thermal component [52]. Apart from the much larger volume of affected tissue in our study (compared to animal studies), it is also possible that the thermal component slows down the resolution of IRE lesion.

Our model is designed to compute the electric field distribution at the time of treatment. We conclude that the threshold of 900 V/cm determined in our study does not represent the actual biological manifestation of IRE which would be beneficial for treatment planning. Our results indicate that lesions visible on MRI 6 weeks post IRE represent tissue areas that experienced a local electric field strength of 900 V/cm or higher during treatment. We hypothesize that a more beneficial correlation with contours at lower electric field thresholds (e.g., 500-700 V/cm) would be achieved if follow up at an earlier time point were available for comparison with simulated ablation volumes. Kos *et al*. [12] compared simulated electric field distribution with findings from contrast enhanced CT on the day of IRE procedure and achieved good overlap with the ablation volume at 700 V/cm threshold. Gallinato *et al*. [15] compared simulated electric field distribution with MRI findings 3 days after IRE procedure and achieved a good fit between isocontours at 500 V/cm threshold and the hypo-enhanced area seen on T1w MRI. Based on the collective knowledge on the estimated threshold for IRE of hepatic tissue and MRI findings from Barabasch *et al*. and Padia *et al*. we assume the best time point for comparison with our computed results would be somewhere between 1 to 2 weeks after IRE procedure. Based on the results of a similar study on RFA of hepatic tumors, an AAE of <4 mm between simulated and actual (segmented) ablation volume should be sufficient for clinical demands and would effectively validate the numerical model.

A future prospective study utilizing multiple follow-up examinations, for example 3 to 5 days (when the inflammation should already subsided), 1 week and 2 weeks post IRE, would enable comparison of computed electric field to ablation size at different time points post IRE and would allow the determination of a more realistic electric field threshold beneficial for treatment planning. However, such a study might be ethically questionable due to repeated exposure of patients to contrast media and would also be quite costly. When a better time point for follow-up image acquisition is determined, a validation of the model performance and sensitivity should be performed in a prospective study and on a larger sample of patients including various liver diseases. Diffusion weighted imaging (DWI) was shown to represent the electroporated zone in early MRI quite well [53] and it does not require a contrast agent or radiation, so it could potentially present a possible solution for multiple follow-up sessions. Another recent pre-clinical study investigated the

trans-catheter intra-arterial perfusion MRI (TRIP-MRI) as a potential biomarker for differentiating reversibly and irreversibly electroporated zones. The study showed promising results in rabbit liver and warrants further investigation [54].

When interpreting the computed results we must, however, also consider the limitations of the numerical models currently in use, which mainly stem from uncertainties in the electrical properties of biological tissues. Whereas electrical conductivities of normal tissues have been measured abundantly (although with a large dispersion of values), properties of various malignant tissues, especially at low frequencies, are still reported with considerable uncertainty. Furthermore, the dynamics and extent of electrical conductivity increase during electroporation are still not well determined and are being actively studied [55]. The retrospective nature of our study is a major drawback and largely contributes to the error in our results. The reconstruction process was limited by missing documentation on needle positions and administered pulse protocols (see "Case selection" section of Materials and Methods), the follow-up intervals were different between patients, image registration (especially multimodal) also produces a certain error. The variance in dielectric properties of tissues and possible errors in the reconstruction of active electrode pairs affects the error in computed electric current (Table I). In a future prospective study, complete imaging of all needle positions (including retracted needles), as well as correct needle numbering would need to be recorded. Lastly, cases that are treated with IRE ablation are usually clinically more challenging, since IRE is still mostly considered only as a "last resort" procedure when other techniques are contraindicated or exhausted. Therefore, a large variance was to be expected in our dataset. In the future, a prospective study would be more appropriate to gather the necessary data to perform a similar analysis and determine a more realistic electric field threshold.

Also investigated in our study was the possible thermal damage due to IRE. Although IRE ablation is considered a non-thermal technique, several studies have shown mild hyperthermic as well as thermal ablation effects during and after IRE [23], [35], [38], [56], [57]. It has been demonstrated that mild hyperthermic effects might even positively affect treatment outcome by presumably lowering the electroporation threshold [58]. However, thermal ablation component could potentially be problematic, since IRE is currently presented as a non-thermal modality for use in cases and anatomical locations, where thermal damage is not acceptable. Our computed results showed considerable heating present in some of the cases – especially in the more clinically challenging cases where many electrodes/pulses were delivered. The highest increase in temperature was observed, as expected, in the vicinity of the electrodes, where the current density is the highest. It is possible, that our model overestimates the extent of thermal damage. Although the Arrhenius equation is quite popular for assessing thermal damage, it is prone to overestimation of cell death at the mild-hyperthermic temperatures, as the kinetic parameters are difficult to define and not well documented for hepatic tissue. Another limitation is the uniform initial perfusion across the tissue, as it underestimates the cooling from the larger blood vessels. Nevertheless, since parts of tissue are cumulatively exposed to hundreds of pulses, undesired heating and thermal necrosis is inevitable, and can negatively affect treatment safety, should the electrodes be in contact or in the immediate vicinity of critical anatomical structures.

Numerical computations and treatment planning in the two selected cases demonstrate the ability to perform IRE ablation without potentially damaging thermal effects. In the two selected cases with a presumably high thermal damage fraction, we were able to eliminate the thermal damage entirely while retaining a complete coverage of the target volume. In this study, only the applied voltage magnitudes were optimized. Another option for decreasing the temperature rise is the reduction of active electrode pairs. Due to uncertainties in ablation zone size, multiple sessions with electrode retraction are often used in clinical practice. In one of the selected cases, we were able to eliminate electrode retraction achieving complete coverage of tumor volume and safety margin in one session, thus also shortening the total procedure time.

Treatment plans in their current realization are usually prepared a few days ahead of intervention using patients' preinterventional imaging. Their usefulness for the interventional radiologist is limited since exact electrode placement according to the plan is often hard to achieve due to anatomical constraints and other technical difficulties. Furthermore, variability in dielectric properties of healthy and tumor tissue directly affect the electric field distribution and therefor influence the treatment efficacy. To ensure that the treatment success is not affected by these factors, a certain safety margin needs to be utilized when preparing the treatment plan. A robustness analysis of the treatment planning for percutaneous IRE is needed to evaluate the impact of errors in electrode positioning and variations in applied voltage and pulses on the effectiveness of the treatment. Despite current limitations, numerical modelling and treatment planning are important tools in understanding and improving electroporation-based treatments. Introduction of numerical treatment planning into clinical practice has the potential to improve the future procedures: we can numerically determine beforehand whether the procedure is feasible or not, optimization of electrode number and active pairs can make the procedure quicker and technically less difficult and the use of lower voltages can avoid high currents and thermal damage. One of the challenges which need to be overcome, however, is the difficulty in placing the electrodes in agreement with the pretreatment plan [59]. Electrode insertion is still mainly performed freehandedly and very few studies can be found where electrode placement is coupled with navigation systems [18], [59]–[61]. We believe combining numerical treatment planning with commercially available navigation systems would even further advance the clinical routine for IRE ablation.

V. Conclusion

In conclusion, the aim of our study was to validate the previously developed numerical framework for the purpose of treatment planning of irreversible electroporation ablation of hepatic tumors – more specifically, to correlate the computed electric field distribution with ablation zone appearance on 6-week follow-up MRI. Our study was limited by its retrospective

nature and a rather late time of follow-up imaging, as the ablation zone has presumably already shrunk in the 6 weeks following the ablation. Since the numerical model is intended to compute the ablation size on the day of treatment, a large error is present in the results and we were therefore not able to effectively validate the model. However, our results indicate that lesions visible on MRI 6 weeks post IRE represent tissue areas that experienced a local electric field strength of 900 V/cm or higher during treatment. Furthermore, we developed and polished a sophisticated method for validation of the numerical treatment planning software. Based on our findings, a future prospective study can be effectively designed, therefore providing the necessary data to further validate the model and ensure sufficient accuracy for clinical demands. A complete database, containing all image segmentations, computed 3D electric field distributions, and 3D surface models of liver, tumors and ablation volumes is also available in the supplementary materials.

Acknowledgment

The authors would like to thank Lukas Lürken, for his help in gathering the missing patient data and for verification of tissue segmentation. The study was conducted within the Infrastructural Centre "Cellular Electrical Engineering", which is part of the Network of Research and Infrastructural Centres of University of Ljubljana (MRIC UL IP-0510).

References

[1] R. V. Davalos *et al.*, "Tissue ablation with irreversible electroporation," *Ann. Biomed. Eng.*, vol. 33, no. 2, pp. 223–231, Feb. 2005.

[2] T. Kotnik *et al.*, "Membrane electroporation and electropermeabilization: Mechanisms and models," *Annu. Rev. Biophys.*, vol. 48, pp. 63–91, May. 2019.

[3] M. L. Yarmush *et al.*, "Electroporation-based technologies for medicine: Principles, applications, and challenges," *Annu. Rev. Biomed. Eng.*, vol. 16, pp. 295–320, Jul. 2014, doi: 10.1146/annurev-bioeng-071813-104622.

[4] L. Rems and D. Miklavčič, "Tutorial: Electroporation of cells in complex materials and tissue," *J. Appl. Phys.*, vol. 119, no. 20, May 2016, Art. no. 201101, doi: 10.1063/1.4949264.

[5] H. J. Scheffer *et al.*, "Irreversible electroporation for nonthermal tumor ablation in the clinical setting: A systematic review of safety and efficacy," *J. Vasc. Interv. Radiol. JVIR*, vol. 25, no. 7, pp. 997–1011, Jul. 2014, doi: 10.1016/j.jvir.2014.01.028.

[6] M. R. Meijerink *et al.*, Eds., *Irreversible Electroporation in Clinical Practice*. Cham, Switzerland: Springer International Publishing, 2018.

[7] K. N. Aycock and R. V. Davalos, "Irreversible electroporation: Background, theory, and review of recent developments in clinical oncology," *Bioelectricity*, vol. 1, no. 4, pp. 214–234, Dec. 2019, doi: 10.1089/bioe.2019.0029.

[8] B. Geboers *et al.*, "High-Voltage electrical pulses in oncology: Irreversible electroporation, electrochemotherapy, gene electrotransfer, electrofusion, and electroimmunotherapy," *Radiology*, vol. 295, no. 2, pp. 254–272, May 2020, doi: 10.1148/radiol.2020192190.

[9] M. Distelmaier *et al.*, "Midterm safety and efficacy of irreversible electroporation of malignant liver tumors located close to major portal or hepatic veins," *Radiology*, vol. 285, no. 3, pp. 1023–1031, Aug. 2017, doi: 10.1148/radiol.2017161561.

[10] N. Verloh *et al.*, "Similar complication rates for irreversible electroporation and thermal ablation in patients with hepatocellular tumors," *Radiol. Oncol.*, vol. 53, no. 1, pp. 116–122, Mar. 2019, doi: 10.2478/raon-2019-0011.

[11] E. I. Cohen *et al.*, "Technology of irreversible electroporation and review of its clinical data on liver cancers," *Expert Rev. Med. Devices*, vol. 15, no. 2, pp. 99–106, Feb. 2018, doi: 10.1080/17434440.2018.1425612.

[12] B. Kos *et al.*, "Careful treatment planning enables safe ablation of liver tumors adjacent to major blood vessels by percutaneous irreversible electroporation (IRE)," *Radiol. Oncol.*, vol. 49, no. 3, pp. 234–241, Sep. 2015, doi: 10.1515/raon-2015-0031.

[13] M. Marčan *et al.*, "Effect of blood vessel segmentation on the outcome of electroporation-based treatments of liver tumors," *PLoS ONE*, vol. 10, no. 5, May 2015, Art. no. e0125591, doi: 10.1371/journal.pone.0125591.

[14] R. Qasrawi *et al.*, "Anatomically realistic simulations of liver ablation by irreversible electroporation: Impact of blood vessels on ablation volumes and undertreatment," *Technol. Cancer Res. Treat.*, vol. 16, no. 6, pp. 783–792, Dec. 2017, doi: 10.1177/1533034616687477.

[15] O. Gallinato *et al.*, "Numerical workflow of irreversible electroporation for deep-seated tumor," *Phys. Med. Biol.*, vol. 64, no. 5, Mar. 2019, Art. no. 055016, doi: 10.1088/1361-6560/ab00c4.

[16] G. Pucihar *et al.*, "Equivalent pulse parameters for electroporation," *IEEE Trans. Biomed. Eng.*, vol. 58, no. 11, pp. 3279–3288, Nov. 2011, doi: 10.1109/TBME.2011.2167232.

[17] Z. Qin *et al.*, "Irreversible electroporation: An in vivo study with dorsal skin fold chamber," *Ann. Biomed. Eng.*, vol. 41, no. 3, pp. 619–629, Mar. 2013, doi: 10.1007/s10439-012-0686-1.

[18] L. P. Beyer *et al.*, "Stereotactically-navigated percutaneous irreversible electroporation (IRE) compared to conventional IRE: A prospective trial," *PeerJ*, vol. 4, Aug. 2016, Art. no. e2277, doi: 10.7717/peerj.2277.

[19] L. P. Beyer *et al.*, "Evaluation of a robotic system for irreversible electroporation (IRE) of malignant liver tumors: Initial results," *Int. J. Comput. Assist. Radiol. Surg.*, vol. 12, no. 5, pp. 803–809, May 2017, doi: 10.1007/s11548-016-1485-1.

[20] R. C. G. Martin *et al.*, "Irreversible electroporation in locally advanced pancreatic cancer: A call for standardization of energy delivery," *J. Surg. Oncol.*, vol. 114, no. 7, pp. 865–871, Dec. 2016, doi: 10.1002/jso.24404.

[21] E. M. Dunki-Jacobs *et al.*, "Evaluation of resistance as a measure of successful tumor ablation during irreversible electroporation of the pancreas," *J. Amer. College Surg.*, vol. 218, no. 2, pp. 179–187, Feb. 2014, doi: 10.1016/j.jamcollsurg.2013.10.013.

[22] A. H. Ruarus *et al.*, "Conductivity rise during irreversible electroporation: True permeabilization or heat?," *Cardiovasc. Intervent. Radiol.*, vol. 41, no. 8, pp. 1257–1266, Aug. 2018, doi: 10.1007/s00270-018-1971-7.

[23] E. M. Dunki-Jacobs *et al.*, "Evaluation of thermal injury to liver, pancreas and kidney during irreversible electroporation in an in vivo experimental model," *Brit. J. Surg.*, vol. 101, no. 9, pp. 1113–1121, Aug. 2014, doi: 10.1002/bjs.9536.

[24] M. Faroja *et al.*, "Irreversible electroporation ablation: Is all the damage nonthermal?," *Radiology*, vol. 266, no. 2, pp. 462–470, Feb. 2013, doi: 10.1148/radiol.12120609.

[25] P. G. K. Wagstaff *et al.*, "Irreversible electroporation of the porcine kidney: Temperature development and distribution," *Urol. Oncol. Seminars Original Investigations*, vol. 33, no. 4, pp. 168.e1–168.e7, Apr. 2015, doi: 10.1016/j.urolonc.2014.11.019.

[26] P. A. Garcia *et al.*, "Predictive therapeutic planning for irreversible electroporation treatment of spontaneous malignant glioma," *Med. Phys.*, vol. 44, no. 9, pp. 4968–4980, Jun. 2017, doi: 10.1002/mp.12401.

[27] M. Marčan *et al.*, "Web-based tool for visualization of electric field distribution in deep-seated body structures and planning of electroporation-based treatments," *Biomed. Eng. Online*, vol. 14, pp. 1–13, Aug. 2015, doi: 10.1186/1475-925X-14-S3-S4.

[28] B. Kos *et al.*, "Robustness of treatment planning for electrochemotherapy of deep-seated tumors," *J. Membrane Biol.*, vol. 236, no. 1, pp. 147–153, Jul. 2010, doi: 10.1007/s00232-010-9274-1.

[29] A. Županič *et al.*, "Treatment planning of electroporation-based medical interventions: Electrochemotherapy, gene electrotransfer and irreversible electroporation," *Phys. Med. Biol.*, vol. 57, no. 17, pp. 5425–5440, Sep. 2012, doi: 10.1088/0031-9155/57/17/5425.

[30] D. Miklavčič *et al.*, "Towards treatment planning and treatment of deep-seated solid tumors by electrochemotherapy," *Biomed. Eng. OnLine*, vol. 9, pp. 10, Feb. 2010, doi: 10.1186/1475-925X-9-10.

[31] P. A. Yushkevich *et al.*, "User-guided 3D active contour segmentation of anatomical structures: Significantly improved efficiency and reliability," *NeuroImage*, vol. 31, no. 3, pp. 1116–1128, Jul. 2006, doi: 10.1016/j.neuroimage.2006.01.015.

[32] J. F. Edd and R. V. Davalos, "Mathematical modeling of irreversible electroporation for treatment planning," *Technol. Cancer Res. Treat.*, vol. 6, no. 4, pp. 275–286, Aug. 2007, doi: 10.1177/153303460700600403.

[33] D. Šel *et al.*, "Sequential finite element model of tissue electropermeabilization," *IEEE Trans. Biomed. Eng.*, vol. 52, no. 5, pp. 816–827, May 2005, doi: 10.1109/TBME.2005.845212.

[34] H. H. Pennes, "Analysis of tissue and arterial blood temperatures in the resting human forearm," *J. Appl. Physiol.*, vol. 85, no. 2, pp. 93–122, Aug. 1948, doi: 10.1152/jappl.1948.1.2.93.

[35] P. Agnass *et al.*, "Mathematical modeling of the thermal effects of irreversible electroporation for in vitro, in vivo, and clinical use: A systematic review," *Int. J. Hyperth.*, vol. 37, no. 1, pp. 486–505, Apr. 2020, doi: 10.1080/02656736.2020.1753828.

[36] N. Pavšelj *et al.*, "The course of tissue permeabilization studied on a mathematical model of a subcutaneous tumor in small animals," *IEEE Trans. Biomed. Eng.*, vol. 52, no. 8, pp. 1373–1381, Aug. 2005, doi: 10.1109/TBME.2005.851524.

[37] T. Jarm *et al.*, "Antivascular effects of electrochemotherapy: Implications in treatment of bleeding metastases," *Expert Rev. Anticancer Ther.*, vol. 10, no. 5, pp. 729–746, May 2010, doi: 10.1586/era.10.43.

[38] P. A. Garcia *et al.*, "A numerical investigation of the electric and thermal cell kill distributions in electroporation-based therapies in tissue," *PloS One*, vol. 9, no. 8, Aug. 2014, Art. no. e103083, doi: 10.1371/journal.pone.0103083.

[39] C. Rossmanna and D. Haemmerich, "Review of temperature dependence of thermal properties, dielectric properties, and perfusion of biological tissues at hyperthermic and ablation temperatures," *Crit. Rev. Biomed. Eng.*, vol. 42, no. 6, pp. 467–492, May 2014.

[40] J. A. Pearce, "Relationship between arrhenius models of thermal damage and the CEM 43 thermal dose," in *Proc. Energy-based Treat. Tissue Assess. V*, Feb. 2009, pp. 718104, doi: 10.1117/12.807999.

[41] O. Gallinato *et al.*, "Numerical modelling challenges for clinical electroporation ablation technique of liver tumors," *Math. Model. Nat. Phenom.*, vol. 15, pp. 1–18, Feb. 2020, doi: 10.1051/mmnp/2019037.

[42] R. E. Neal *et al.*, "In vivo irreversible electroporation kidney ablation: Experimentally correlated numerical models," *IEEE Trans. Biomed. Eng.*, vol. 62, no. 2, pp. 561–569, Feb. 2015, doi: 10.1109/TBME.2014.2360374.

[43] R. E. Neal *et al.*, "Improved local and systemic anti-tumor efficacy for irreversible electroporation in immunocompetent versus immunodeficient mice," *PloS One*, vol. 8, no. 5, May 2013, Art. no. e64559, doi: 10.1371/journal.pone.0064559.

[44] V. M. Ringel-Scaia *et al.*, "High-frequency irreversible electroporation is an effective tumor ablation strategy that induces immunologic cell death and promotes systemic anti-tumor immunity," *EBioMedicine*, vol. 44, pp. 112–125, Jun. 2019, doi: 10.1016/j.ebiom.2019.05.036.

[45] C. Bastianpillai *et al.*, "Harnessing the immunomodulatory effect of thermal and non-thermal ablative therapies for cancer treatment," *Tumor Biol.,* vol. 36, no. 12, pp. 9137–9146, Dec. 2015, doi: 10.1007/s13277-015-4126-3.

[46] H. J. Scheffer *et al.*, "Irreversible electroporation of locally advanced pancreatic cancer transiently alleviates immune suppression and creates a window for antitumor t cell activation," *Oncoimmunology*, vol. 8, no. 11, Aug. 2019, Art. no. 1652532, doi: 10.1080/2162402X.2019.1652532.

[47] T. Polajzer *et al.*, "Analysis of damage-associated molecular pattern molecules due to electroporation of cells in vitro," *Radiol. Oncol.*, vol. 54, no. 3, pp. 317–328, Jul. 2020, doi: 10.2478/raon-2020-0047.

[48] M. Moche *et al.*, "Clinical evaluation of in silico planning and real-time simulation of hepatic radiofrequency ablation (ClinicIMPPACT trial)," *Eur. Radiol.*, vol. 30, no. 2, pp. 934–942, Feb. 2020, doi: 10.1007/s00330-019-06411-5.

[49] A. Barabasch *et al.*, "Magnetic resonance imaging findings after percutaneous irreversible electroporation of liver metastases: A systematic longitudinal study," *Invest. Radiol.*, vol. 52, no. 1, pp. 23–29, Jan. 2017, doi: 10.1097/RLI.0000000000000301.

[50] S. A. Padia *et al.*, "Irreversible electroporation in patients with hepatocellular carcinoma: Immediate versus delayed findings at MR imaging," *Radiology*, vol. 278, no. 1, pp. 285–294, Jan. 2016, doi: 10.1148/radiol.2015150031.

[51] M. Kranjc *et al.*, "In situ monitoring of electric field distribution in mouse tumor during electroporation," *Radiology*, vol. 274, no. 1, pp. 115–123, Jan. 2015, doi: 10.1148/radiol.14140311.

[52] J. A. Vogel *et al.*, "Time-Dependent impact of irreversible electroporation on pancreas, liver, blood vessels and nerves: A systematic review of experimental studies," *PloS One*, vol. 11, no. 11, 2016, Art. no. e0166987, doi: 10.1371/journal.pone.0166987.

[53] F. Mahmood *et al.*, "Diffusion-weighted MRI for verification of electroporation-based treatments," *J. Membrane Biol.*, vol. 240, no. 3, pp. 131–138, Apr. 2011, doi: 10.1007/s00232-011-9351-0.

[54] L. Pan *et al.*, "Transcatheter intraarterial perfusion MRI approaches to differentiate reversibly electroporated penumbra from irreversibly electroporated zones in rabbit liver," *Acad. Radiol.*, vol. 27, no. 12, pp. 1727–1733, Dec. 2020, doi: 10.1016/j.acra.2020.01.008.

[55] Y. Zhao *et al.*, "Development of a multi-pulse conductivity model for liver tissue treated with pulsed electric fields," *Front. Bioeng. Biotechnol.*, vol. 8, May 2020, doi: 10.3389/fbioe.2020.00396, Art. no. 396.

[56] W. van den Bos *et al.*, "Thermal energy during irreversible electroporation and the influence of different ablation parameters," *J. Vasc. Interv. Radiol. JVIR*, vol. 27, no. 3, pp. 433–443, Mar. 2016, doi: 10.1016/j.jvir.2015.10.020.

[57] T. J. O'Brien *et al.*, "Effects of internal electrode cooling on irreversible electroporation using a perfused organ model," *Int. J. Hyperth.*, vol. 35, no. 1, pp. 44–45, May 2018, doi: 10.1080/02656736.2018.1473893.

[58] C. M. Edelblute *et al.*, "Controllable moderate heating enhances the therapeutic efficacy of irreversible electroporation for pancreatic cancer," *Sci. Rep.*, vol. 7, no. 1, Sep. 2017, Art. no. 11767, doi: 10.1038/s41598-017-12227-4.

[59] I. Fuhrmann *et al.*, "Navigation systems for treatment planning and execution of percutaneous irreversible electroporation," *Technol. Cancer Res. Treat.*, vol. 17, Jan. 2018, Art. no. 1533033818791792, doi: 10.1177/1533033818791792.

[60] A. Grošelj *et al.*, "Coupling treatment planning with navigation system: A new technological approach in treatment of head and neck tumors by electrochemotherapy," *Biomed. Eng. Online*, vol. 14, pp. 1–14, Sep. 2015, doi: 10.1186/1475-925X-14-S3-S2.

[61] L. P. Beyer *et al.*, "Evaluation of a robotic system for irreversible electroporation (IRE) of malignant liver tumors: Initial results," *Int. J. Comput. Assist. Radiol. Surg.*, vol. 12, no. 5, pp. 803–809, May 2017, doi: 10.1007/s11548-016-1485-1.